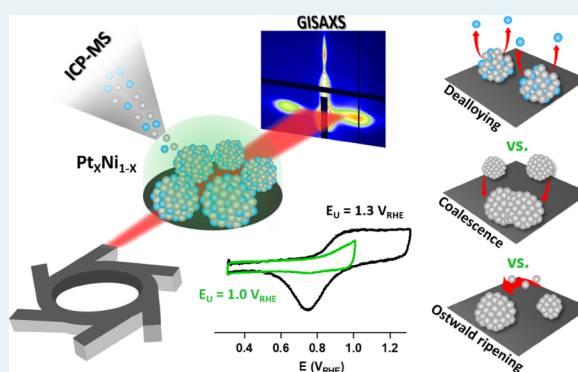


Interplay Among Dealloying, Ostwald Ripening, and Coalescence in $\text{Pt}_x\text{Ni}_{100-x}$ Bimetallic Alloys under Fuel-Cell-Related Conditions

Marco Bogar, Yurii Yakovlev, Daniel John Seale Sandbeck, Serhiy Cherevko, Iva Matolínová, Heinz Amenitsch,* and Ivan Khalakhan*

ABSTRACT: Platinum-based bimetallic alloys have been largely investigated during the last few years as a valid alternative to bare Pt cathode catalysts for proton-exchange membrane fuel cells (PEMFCs) to improve their cost-efficiency. Nonetheless, Pt bimetallic alloys are characterized by a reduced stability, which is poorly understood at a fundamental level. It is thus essential to describe the entire chain of interconnected degradation mechanisms to formulate a comprehensive model of catalyst degradation that will help interpret bimetallic alloy behavior in real complex fuel cell systems. By combining *in situ* inductively coupled plasma mass spectroscopy, *in situ* grazing-incidence small-angle X-ray scattering, and *ex situ* scanning electron microscopy, we have studied the morphological evolution of $\text{Pt}_x\text{Ni}_{100-x}$ model catalysts with different Ni contents (ranging from 0 to 75%) undergoing potentiodynamic cycling to two different upper potentials mimicking the different operational conditions of a PEMFC: 1.0 and 1.3 V_{RHE} . Data analysis allowed us to develop a methodology to distinguish the influence of Ni dissolution, particle coalescence, and Ostwald ripening on particle size distribution and interparticle distance and to realize time-dependent interplay maps to highlight the timeframe in which the aforementioned phenomena are prevailing or coexisting. Results show that Ni dissolution is the only phenomenon inducing morphological evolution when the lower upper potential is chosen. On the contrary, at 1.3 V_{RHE} , Ni dissolution is rapidly overcome by particle coalescence at first and by Ostwald ripening in the later stages of the investigated time range. The onset of every phenomenon was found to occur earlier in time for larger values of Ni concentrations.

KEYWORDS: fuel cells, bimetallic catalyst dealloying, degradation, *in situ* grazing-incidence small-angle X-ray scattering, particle coalescence, Ostwald ripening



■ INTRODUCTION

Proton-exchange membrane fuel cells (PEMFCs) are one of the most promising candidates for leading the transition from energy production methods based on fossil fuels to zero-emission technologies. However, a large-scale deployment of PEMFCs into the market is still hampered due to several shortcomings, among which high catalyst cost and stability are the most prominent.

While technology has now started reaching cost-efficient targets by replacing conventional platinum catalysts with platinum alloys with cheaper transition metals,¹⁻⁶ the problem remains with durability because of their higher susceptibility to corrosion and deactivation. Complex bimetallic systems have been found to lose their superficial structure and chemical integrity due to the harsh conditions in the PEMFC cathode, such as the relatively high potentials and low pH.⁷⁻¹² To date, several different processes have been identified causing reduction of performance of fuel cells assembled with benchmark Pt/C nanoparticle catalysts.¹³⁻¹⁵ Corrosion of the carbon support and platinum dissolution were found to act

as primary sources of degradation, triggering a set of secondary degradation mechanisms like particle detachment, particle agglomeration (coalescence), and Ostwald ripening.^{13,14} The latter two are responsible for a gradual increase of catalyst nanoparticle size, resulting in a reduction of the active surface area and consequently a decrease in fuel cell efficiency. In turn, in the case of a binary PtM system (with M being a transition metal), faster dissolution of the less noble metal due to high overpotentials introduces a second degree of freedom, further affecting catalyst degradation pathways. These additional phenomena strongly depend on the alloy composition.^{16,17} Moreover, dissolved transition metals were proven to block transport pathways for ions in ionomers and membranes,

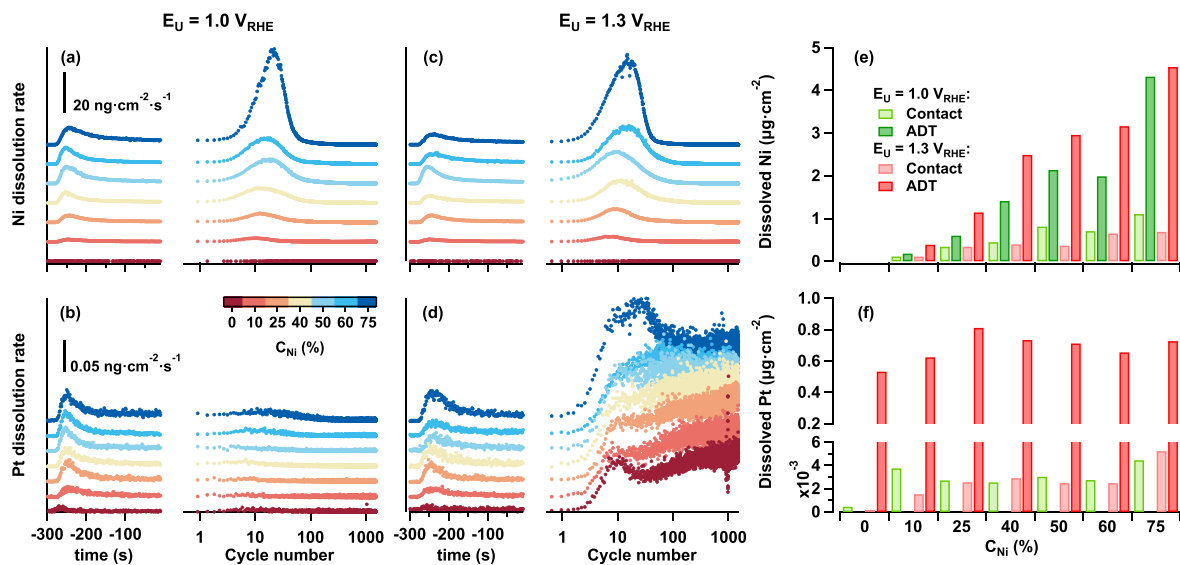


Figure 1. ICP-MS. Variation of (a, c) Ni and (b, d) Pt contact dissolution rates in contact with the electrolyte versus time and during potentiodynamic cycling (1500 cycles) for (a) Ni and (b) Pt at the upper potential (E_U) equal to $1.0 V_{RHE}$ and for (c) Ni and (d) Pt at E_U equal to $1.3 V_{RHE}$. For clarity, traces in (a)–(d) have been vertically shifted. Total amount of (e) Ni and (f) Pt dissolved in contact with the electrolyte and during cyclic voltammetry for both upper potentials.

further adversely affecting PEMFC performance.^{18,19} Thus, it becomes essential to describe the entire chain of interconnected degradation mechanisms during catalyst operation to formulate a comprehensive model of catalyst degradation and possibly develop a corresponding mitigation strategy leading toward a more robust catalyst.

It is generally expected that at higher potentials, the enhanced Pt dissolution makes Ostwald ripening the most favorable mechanism. On the other hand, at lower potentials, nanoparticle migration and coalescence are likely to occur. However, more and more studies have revealed that both coalescence and Ostwald ripening coexist during electrochemical aging of the catalyst.^{20–22} A clear distinction between concurrent coarsening effects is thus experimentally challenging and has been the topic of a long-standing debate and controversial conclusions.^{23,24} In the past, the shape of the nanoparticle size distribution determined by analysis of microscopic images has been used as an indirect diagnostic tool to obtain insight into the underlying coarsening mechanism by juxtaposing it with well-established theoretical models for Ostwald ripening and coalescence.^{25,26} However, the experimental errors together with relatively poor statistics of local microscopy techniques limited the formulation of a reliable conclusion. Moreover, for an extended period, most microscopic methods have been unable to measure changes in the catalyst morphology *in situ* during the electrochemical treatment, limiting information to the initial and final stages only. As a complementary and/or alternative method, attention was then paid to the use of *in situ* small-angle X-ray scattering (SAXS) to monitor the morphological evolution of the catalyst undergoing specific electrochemical reactions with high resolution and high statistical accuracy.^{21,27–32}

Nevertheless, to the best of our knowledge, there is no clear experimental evidence in the literature for accurate discrimination of different coarsening mechanisms during electrochemical degradation of platinum or platinum-based alloy catalysts, which can be related to the fact that models describing a single process cannot be used for evaluating

nanoparticle size distribution when both of the processes are taking place concurrently.^{22,33}

Herein, we present a comprehensive study on time-resolved degradation of Pt–Ni catalysts in a half-cell as a function of the alloy composition and electrode potential. To enable application of powerful *in situ* surface science techniques and at the same time to mimic real nanoparticulate catalysts, well-defined model catalytic systems consisting of homogeneously distributed assemblies of Pt–Ni catalyst grains deposited onto a Si(111) substrate (precovered by a thin layer of carbon) were used.³⁴ Seven different Pt-to-Ni ratios (Pt_xNi_{100-x} , $0 \leq x \leq 100$) were tested *in situ* during potentiodynamic cycling to a different upper potential (1.0 and $1.3 V$ with respect to the reversible hydrogen electrode, RHE), known to cause substantially different degrees of Pt dissolution.³⁵ To retrieve online information about dissolution rates of Pt and Ni as well as total amounts of dissolved metals during electrochemical cycling, an electrochemical scanning flow cell (SFC) with online detection by inductively coupled plasma mass spectrometry (ICP-MS) was employed. *In situ* electrochemical grazing-incidence small-angle X-ray scattering (GISAXS)³⁶ was further used to provide in-depth mean morphological variation of the catalyst as a function of time and alloy composition. In this way, recording statistically meaningful microscopic parameters, the different processes affecting catalyst stability were observed and discriminated.

RESULTS AND DISCUSSION

The dealloying of the investigated samples was studied at first using the SFC coupled to ICP-MS. Results from *in situ* mass spectrometry are summarized in Figure 1. Figure 1a–d shows the dissolution rates for Ni and Pt plotted as a function of time after contacting the sample prior to cycling voltammetry (so-called contact dissolution) and as a function of cycle number during potentiodynamic cycling to the upper potentials (E_U) of $1.0 V_{RHE}$ (denoted mild conditions) and $1.3 V_{RHE}$ (denoted harsh conditions) for each Pt–Ni composition. In turn, total amounts of dissolved Ni and Pt are compared in Figure 1e,f,

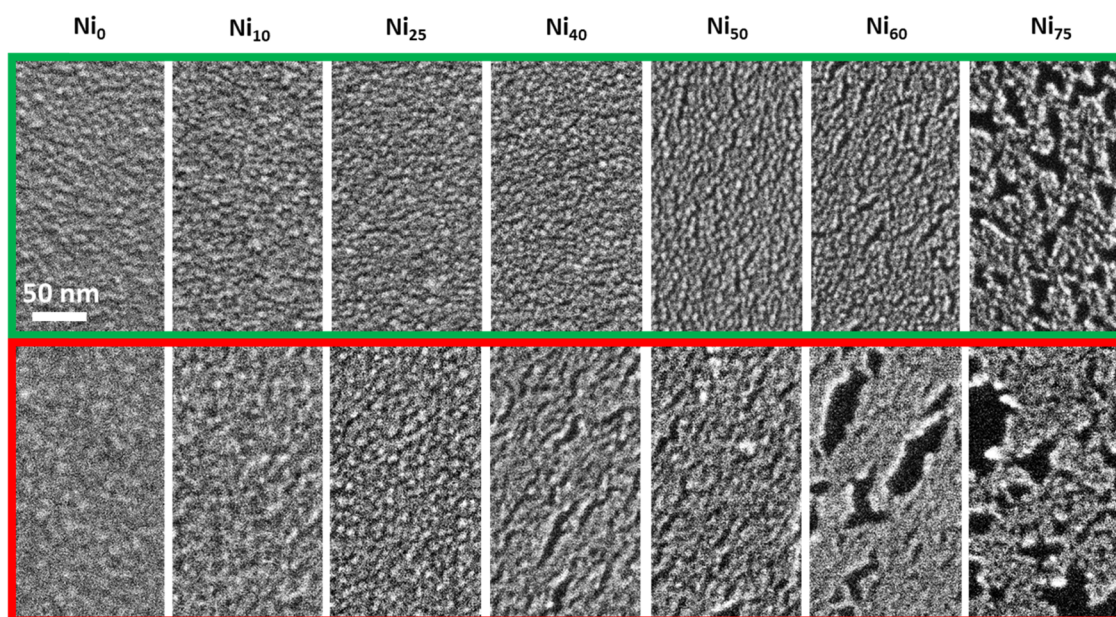


Figure 2. *Ex situ* SEM. Comparison between the final state of samples cycled over 1500 CV cycles at E_U equal to $1.0 V_{RHE}$ (mild conditions, top) and $1.3 V_{RHE}$ (harsh conditions, bottom) as a function of Ni concentration.

respectively. The corresponding CV curves are shown in [Figures S1 and S2](#).

Both Ni contact dissolution and Ni dissolution during cyclic voltammetry at mild conditions were observed and, as expected, the Ni dissolution rate increases with increasing Ni content within the sample ([Figure 1a](#)). This is in agreement with the thermodynamic stability of Ni in this potential and pH range.³⁷ The massive contact dissolution from Ni seen in all samples emphasizes the need for preleaching during catalyst synthesis, in particular before the catalyst is brought into contact with the ionomer material, to prevent detrimental ionomer poisoning.^{18,19} Pt dissolution ([Figure 1b](#)) is only seen upon contact of the working electrode; however, the initial stages of potential cycling and the so-called contact dissolution do not fit any particular trend based on the composition of the sample, which can be attributed to varying degrees of surface oxidation simply due to the sample exposition to air.³⁸ When cyclic voltammetry is performed, in accordance with the Ni dissolution rates, a small amount of dissolved Pt is detected within the first 100 cycles. This behavior can be related to the increased surface area,³⁹ which is a consequence of the significant Ni dissolution, exposing low-coordinated Pt sites susceptible to dissolution.^{40,41} After a few hundred cycles, both Pt and Ni dissolution rates fall to zero, as a Pt-rich surface layer develops from the significant dissolution of Ni. This Pt-rich surface layer is highly stable toward dissolution in this potential range with limited oxide formation and reduction and prevents further Ni leaching.^{14,35,42}

When increasing the upper potential limit to $1.3 V_{RHE}$ (harsh conditions), Ni dissolution rates and quantities ([Figure 1c,e](#), respectively) are again greater than for Pt ([Figure 1d,f](#)) by approximately one order of magnitude. The most significant Ni dissolution is observed at the initial stages of the stress tests (about within the first 100 cycles) although Ni dissolution rates remain above baseline values until the end of the potential cycling. In addition, the amount of dissolved Ni is more consistent with increasing Ni content both during contact conditions and when performing cyclic voltammetry.

At low Ni contents, for Ni concentrations (C_{Ni}) ranging from 0 up to 25%, both the dissolution rate and the amount of dissolved Pt show an increasing trend as a function of C_{Ni} ; in fact, larger amounts of dissolved Ni increase the Pt surface, which is exposed to the electrolyte. However, as the Pt content is further reduced, Pt dissolution decreases and similar rates and quantities are observed. We relate this fact to a trade-off, which is set in between the increase of the exposed surface area (due to Ni dissolution) and the decrease of the Pt content (due to Pt dissolution). Finally, for C_{Ni} equal to 75%, the Pt dissolution rate peaks within the first 100 cycles, which coincides with extremely high Ni dissolution rates (and the very high surface area of Pt). In such conditions, Pt dissolves during cyclic voltammetry due to oxide formation, its reduction, and the interrelated place-exchange mechanism.^{14,29,35,42}

The effects of metal dissolution as a function of Ni concentration were investigated by postmortem, *ex situ* scanning electron microscopy (SEM), summarized in [Figure 2](#). After cycling at E_U equal to $1.0 V_{RHE}$, no noticeable changes in the samples with Ni concentration ranging from 0 to 40% could be detected. At C_{Ni} equal to 50%, some short grooves can be seen. These features evolve to cracks for higher nickel contents, and their formation can be related to the large amount of dissolved Ni.^{9,30} When the upper potential is set to $1.3 V_{RHE}$, grooves and cracks can be observed when C_{Ni} is higher than 40%.

In situ GISAXS was further employed to investigate the morphological changes in the in-plane (horizontal) and out-of-plane (vertical) directions. A comparison of the horizontal and vertical cuts of corresponding scattering patterns obtained from as-deposited samples just immersed in a liquid electrolyte is shown in [Figure S3](#). Here, due to the different amount of dissolved metal, it can be noticed that sample morphology is dependent on Ni content, as highlighted by the mean particle diameter (D_p , [Figure S3e](#)) and the minimum interparticle distance ($d_{p,min}$, [Figure S3f](#)) values, retrieved by fitting horizontal cuts with the analytical model.

Time-resolved GISAXS horizontal and vertical cuts for the samples cycled at the upper potential of 1.0 V_{RHE} are shown in Figures S4 and S5, respectively. In horizontal cuts, the predominant feature is represented by the peak present at around 1 nm^{-1} , which is related to the spatial arrangement of Pt nanoparticles at the surface. Concerning the vertical cuts, scattering patterns are characterized by the presence of the Kiessig fringes.⁴³ These modulations in the scattering cross-section are caused by the interference of X-rays refracted at the top and bottom interfaces of the metallic layer, and their periodicity is inversely proportional to the thickness of the layer itself.^{44,45} For Ni concentrations ranging from 0% up to 50%, no significant changes could be detected in both cuts. This is in agreement with our previous studies performed on the same model system with C_{Ni} equal to 50%³⁰ and with bare Pt as well.³⁶ On the contrary, for Ni concentrations higher than 50%, the sample morphology evolves once cyclic voltammetry is applied. In particular, the shift toward lower q -values of the peak in the horizontal cut highlights an increase of interparticle distance, while the fading of the intensity of the Kiessig fringes in the vertical cut indicates an increase in sample roughness, a thinning of the catalyst layer, and a local clustering of particles, consistent with SEM observations. After several hundred CV cycles, all nickel that was present within the first few nanometers of the sample surface is dissolved. Subsequent exposure of a skeleton made of bare Pt leads to a halt in surface evolution because the upper potential of 1.0 V_{RHE} is not sufficiently positive to significantly affect the morphology of the platinum nanoparticles.^{29,36}

Once the upper potential is increased to 1.3 V_{RHE} (horizontal and vertical cuts are displayed in Figures S6 and S7, respectively), morphological evolution is even more strongly dependent on the Ni content. Even at low Ni concentrations (0 and 10%), the shift of the peak in the horizontal cut toward lower q -values indicates an increase in the average interparticle distance. From the vertical cut, an increase of the distance between the bumps of the Kiessig fringes can be observed, describing a thinning of the catalyst layer. In addition, the intensity of the fringes decreases rapidly around 1000 CV cycles. The evolution of the vertical cut is more evident when the Ni concentration is increased to 25%. Here, the horizontal cut does not provide significant variations with respect to the samples with lower Ni contents, while in the vertical cut, three stages can be easily distinguished: (i) initial thinning of the sample, revealed by the increase in distance between the bumps of the Kiessig fringes; (ii) increased roughening of the surface, revealed by damping of the fringe intensity; and (iii) disruption of the initial morphology (evident after 1300 CV cycles), followed by the rise of the bump/peak in the low- q -range (in between 0 and 0.5 nm^{-1}). The same trends in horizontal and vertical cuts can also be highlighted for Ni concentrations up to 60%. Finally, at C_{Ni} equal to 75%, the initial morphology of the sample changes completely already within the first 10 CV cycles in both the horizontal and vertical cuts.

Calculated scattering correlation length^{46,47} (Figure S8) was chosen to serve as a qualitative descriptor of the onset of the processes described in the previous paragraphs. Indeed, scattering correlation length (ξ) is related to the grain size and surface roughness and can be used to roughly monitor the average evolution of the morphological changes taking place at the surface, if evaluated along the horizontal cut. In addition, if calculated from the vertical cut, it provides a qualitative

indication of the evolution of the sample thickness. Concerning samples cycled in mild conditions, at C_{Ni} equal to 60%, the dissolution of Ni induces some morphological changes between 10 and a few hundred CV cycles. Here, the Pt skeleton can be considered to be completely exposed when the trend reaches a plateau. On the contrary, at C_{Ni} equal to 75%, it can be defined that the most relevant changes occur within the first five cycles and that the Pt skeleton is fully exposed in between 60 and 100 cycles. These observations match the trends defined by the dissolution profiles of Pt and Ni recorded by ICP-MS (Figure 1). Moreover, when cyclic voltammetry was performed in harsh conditions, the onset of the in-plane morphological evolution is inversely proportional to the Ni concentration, as expected. When the upper potential is set to 1.3 V_{RHE} , the continuous evolution of the scattering correlation length since the very first cycles in both of the cuts (Figure S8) clearly shows that a continuous evolution of the system is taking place along the entire investigated timeframe.

For a more accurate analysis, scattering patterns were fitted by means of the so-called analytical model. Fitting results for the samples cycled in mild and harsh conditions are summarized in Figures S9 and S10, respectively. Because of the large number of parameters retrieved from data fitting, which would increase discussion complexity, the analysis has been focused on three main parameters only: the mean particle diameter D_p , the root-mean-square deviation from particle diameter σ_p , and the (calculated) minimum interparticle distance $d_{p,\text{min}}$. In fact, the changes of the additional parameters composing the analytical model were found to be in agreement with the variation of these three main ones. When the upper potential was set to 1.0 V_{RHE} , the evolution of parameters remains constant for Ni content ranging from 0 up to 25% and relative deviation from the initial value is about a few percentage points only. If the Ni concentration is raised to intermediate values, Ni dissolution is large enough to induce changes in surface morphology. By monitoring the temporal evolution of root-mean-square deviation from particle diameter σ_p (Figure S9c), an initial downward trend can be detected until the profile of the Ni dissolution rate recorded from ICP-MS (Figure 1a) has reached its maximum value. Then, σ_p values rise before stabilizing to a plateau. This trend is almost negligible for C_{Ni} equal to 40%, yet it is evident when the Ni concentration is equal to 50 and 60%. Here, Ni dissolution is also responsible for the reduction of the minimum interparticle distance ($d_{p,\text{min}}$, Figure S9f) and for the relative reduction of the calculated thickness (Figure S9h), which was quantified to be equal to 7 and 8%, respectively. For high Ni concentrations (60 and 75%), Ni dissolution induces an additional decrease in the mean particle size (D_p , Figure S9d) and the reduction of $d_{p,\text{min}}$. Again, the time course of the parameter evolution matches with the time scale of the recorded profile of the Ni dissolution rate (Figure 1a). As a first outcome, we can claim that Ni dissolution is responsible for the reduction of the σ_p value within the first tens of CV cycles when the Ni dissolution rate reaches its maximum value. After this point, an increase in σ_p could be detected together with the decreasing slope in Ni dissolution profiles. For Ni-rich samples, the dissolution of a large amount of the less noble metal induces a more pronounced change, which can be related to the formation and growth of the cracks observed via SEM. Here, the observed results are in accordance with the model proposed by Erlebacher *et al.* describing the dealloying as the complex interplay between selective dissolution of less noble metal and

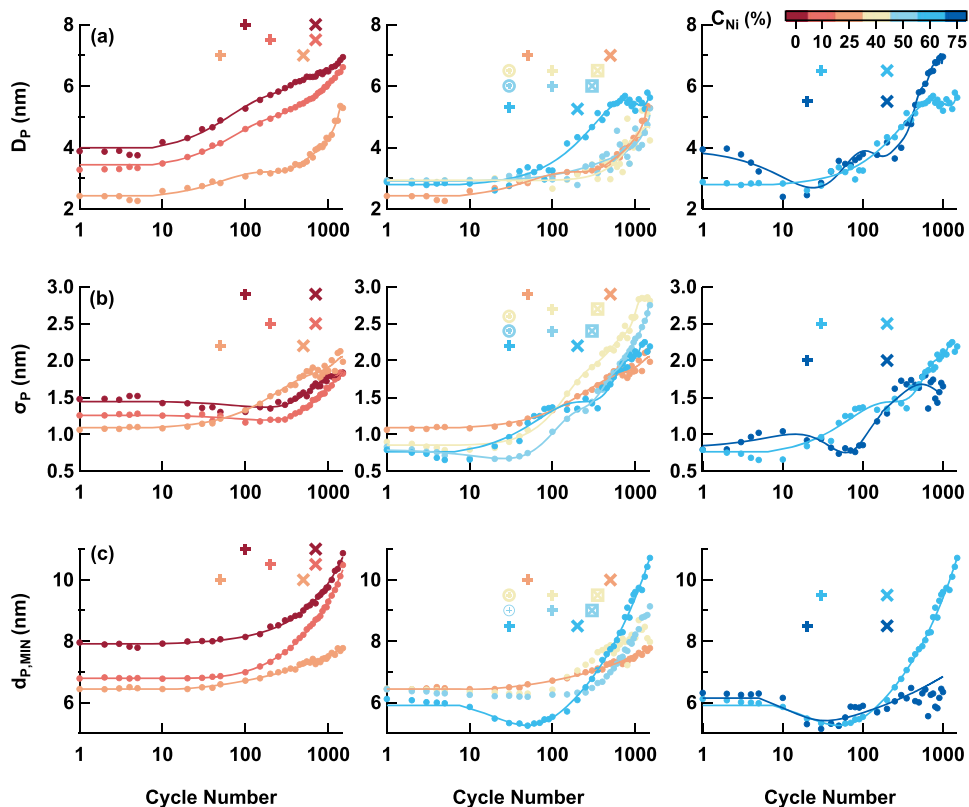


Figure 3. Results of fitting the GISAXS pattern of Pt–Ni samples cycled at E_U equal to $1.3 V_{RHE}$ — main parameters. Time evolution of main parameters obtained from fitting the horizontal cuts, as a function of CV cycle number and for different Ni contents; E_U was set to $1.3 V_{RHE}$. (a) Mean particle diameter D_p , (b) root-mean-square deviation of particle diameter σ_p , and (c) minimum interparticle distance $d_{p,min}$. For a better visualization, traces were divided into (left) low Ni concentrations, (center) medium Ni concentrations, and (right) high Ni concentrations. Marks “+” and “x” highlight the points in which particle coalescence and Ostwald ripening become dominant, respectively. The starting points for Ni dissolution and for Pt redistribution were not indicated for clarity, but they can be considered taking place from the beginning of the measurement. Circled “+” and boxed “x” highlight the starting point of a regime of mixed dissolution and coalescence and mixed coalescence and Ostwald ripening, respectively.

surface diffusion of the remaining low-coordinate noble metal atoms toward more stable sites.¹⁶

Figure 3 shows the variation of the main parameters retrieved from fitting the scattering patterns recorded from samples cycled in harsher conditions at $1.3 V_{RHE}$. Here, in addition to dealloying, more phenomena are involved. As previously observed,^{22,30,36} there are two main processes developing during potentiodynamic cycling: particle coalescence and Ostwald ripening. Both cause an increase in the mean particle diameter D_p and the root-mean-square deviation of the particle diameter σ_p . To distinguish between these two phenomena, we have adopted the following criteria: particle coalescence is predominant when both (i) the mean particle diameter and (ii) its root-mean-square deviation are increasing and when (iii) the shape of the curve representing the probability distribution function of the number-weighted size distribution is skewed toward higher diameter values (under such conditions, the calculated skewness tends to be positive and higher than zero). The increase in particle diameter and σ_p are due to the merging of the adjacent particles composing the initial particle population. As a consequence, an increase in the minimum interparticle distance can be detected. When no clear evidence was found, an intermediate region in which Ni dissolution and particle coalescence are coexisting was established, up to the point in which Ni dissolution ended. From this point, particle coalescence was considered as the

main phenomenon taking place. On the contrary, we have attributed that Ostwald ripening is predominant when (i) an upturn in the increasing trend of the mean particle diameter was observed together with (ii) an upturn in the increasing trend of the minimum interparticle distance.^{30,36} In such conditions, it was noticed that (iii) the shape of the probability distribution function becomes more symmetrical and that the slope of calculated skewness is not increasing. Indeed, an increase in mean particle size is expected due to the disappearance of the smaller particles composing the system, which is the basis of the Ostwald ripening process. As a consequence, an increase in interparticle distance is expected to be observed due to the disappearance of the nearest neighbor particles. In Figure 3, the time-points in which particle coalescence and Ostwald ripening become the predominant coarsening phenomena are marked by the symbols “+” and “x”, respectively, while the shapes of calculated number-weighted size distributions when cyclic voltammetry was carried out at 1.0 and $1.3 V_{RHE}$ are compared in Figures S11 and S12, respectively. Finally, calculated skewness as a function of the cycle numbers is compared in Figure S13.

In the left column of Figure 3, the evolution of the main parameters for the samples having low Ni concentrations (0 and 10%) is shown. After the first 10 CV cycles, an increase in the mean particle diameter, together with a reduction of its

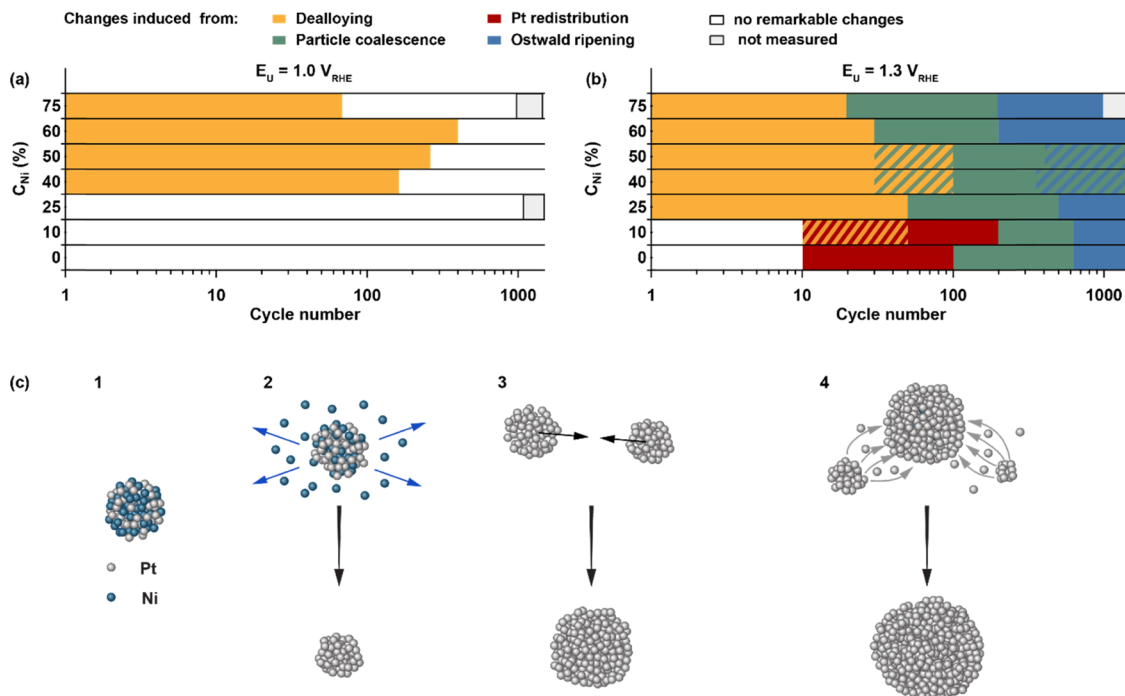


Figure 4. Interplay maps and sketch of the processes involved. Graphical representation of the predominant process as a function of Ni concentration and time (expressed as a function of the number of CV cycles) for Pt–Ni samples cycled at E_U equal to (a) $1.0 V_{RHE}$ and (b) $1.3 V_{RHE}$. (c) Schematic representation of the processes involved in catalyst coarsening: (1) representative Pt–Ni nanoparticle (starting point), (2) dealloying (consisting of Ni dissolution and Pt diffusion), (3) particle coalescence, and (4) Ostwald ripening.

root-mean-square deviation σ_p , is observed. The calculated skewness retrieved from particle size distribution decreases as well. This behavior however does not completely match any of the aforementioned processes. We assume it could be related to a platinum diffusion phenomenon at the beginning of cycling and at very low Ni contents (at higher Ni contents, Ni dissolution is the dominant process). In this manuscript, we will refer to this as Pt redistribution, which is related to the initial fast growth of particle size.^{27,48} For C_{Ni} equal to 10%, we assume that this process is taking place corresponding to the negligible Ni dissolution observed by IPC-MS (Figure 1c). The limited impact of these processes does not allow one to discriminate among them and a mixed regime in which Ni dissolution and Pt redistribution are assumed to rule the morphological evolution of this sample. After 50 CV cycles, only Pt redistribution is assumed to take place because the Ni dissolution profile indicates that no remarkable amounts of dissolved Ni can be detected. After 100 CV cycles, Ni dissolution is ended and, for C_{Ni} equal to 0 and 10%, the Pt dissolution profile reaches a plateau (Figure 1d). Starting from this point, particle coalescence was defined as the predominant phenomenon taking place due to the increase of D_p and σ_p values. For C_{Ni} equal to 10%, this transition point was observed after 200 CV cycles. At this stage, the onset of reduction of the calculated sample thickness (Figure S10h) was spotted. Finally, the predominance of Ostwald ripening can be highlighted around 700 CV cycles, corresponding to the upturn of D_p and to the clear increase of $d_{p,min}$, as also indicated by the evolution of the number-weighted size distribution (Figure S12) as well as from the constant trends in calculated skewness values (Figure S13). By increasing the Ni concentration to 25%, the same trends can be detected to take place earlier in time: the onset of particle coalescence can be spotted after 50 CV cycles, while the predominance of Ostwald ripening can be set after

500 CV cycles, as is clearly underlined by the decreasing trend in calculated skewness (Figure S13; the upturn in $d_{p,min}$ is not sharp in this case). Finally, from the analysis of the vertical cut, the calculated sample thickness was found to be reduced by 10, 11, and 15% from the initial value for C_{Ni} equal to 0, 10, and 25%, respectively. At intermediate Ni contents (C_{Ni} equal to 40 and 50%), the most remarkable effect is a sudden reduction in sample thickness (Figure S10h), which is induced by the larger amount of dissolved Ni. As depicted in the middle column in Figure 3, a sharp distinction between the stages of dissolution and coalescence is observed between 10 and 100 CV cycles cannot be detected, while only an increase in σ_p can be observed. Combining such information with the evolution of Ni and Pt dissolution rates, we can conclude that Ni dissolution and particle coalescence coexist. The onset of these mixed contribution regimes is highlighted by the circled-cross mark in Figure 3. Particle coalescence becomes the leading phenomenon only after dissolution profiles indicate that Ni dissolution stopped, i.e., after 100 CV cycles. Coalescence is also observed during the start in D_p growth, which can be observed at 100 CV cycles. At a later stage of potential cycling, the absence of the upturns in D_p and $d_{p,min}$, together with the observation of the shape of the calculated size distribution (Figure S12d,e), makes us assume that Ostwald ripening and particle coalescence take place simultaneously until the end of the investigated time range. In fact, although D_p and $d_{p,min}$ keep continuously growing, the calculated skewness of particle size distribution keeps increasing up to the end of the investigated range. The final reductions of the calculated sample thickness were detected to be equal to 36 and 29% for C_{Ni} equal to 40 and 50%, respectively. Finally, at high Ni concentrations (Figure 3, right column), dissolution strongly affects the catalyst morphology within the first 20 CV cycles, when most of the Ni is dissolved (Figure 1c) and the profile of the Pt

dissolution rate reaches the plateau region (Figure 1d). From this point, particle coalescence (D_p and σ_p start growing, skewness is increasing) can be considered as the leading phenomenon up to about 200 CV cycles, when the onset for Ostwald ripening (further increase in D_p and $d_{p,min}$, end of increase in the calculated skewness) can be observed. Trends are more clear for C_{Ni} equal to 60%, for which a final reduction of sample thickness equal to 37% could be calculated. Concerning C_{Ni} equal to 75%, the roughly constant trend characterizing σ_p between 20 and 200 CV cycles may be due to the very little amount of Pt present in the sample. It can be expected that particle coalescence is not taking place at a rate that is large enough to reveal remarkable changes in σ_p .

A schematic illustration of the time-dependent interplay between the described processes for the Pt–Ni samples cycled at both upper potentials is summarized in Figure 4. At mild conditions (E_U equal to 1.0 V_{RHE}), morphological evolution is induced by Ni dissolution only and significant morphological variations can be assigned to migration of low-coordinated Pt atoms, as described by Erlebacher *et al.*¹⁶ The temporal evolution of this effect was found to be in agreement with the Ni dissolution profiles (Figure 1), and the severity of the process is largely dependent on the initial Ni concentration (also in agreement with *ex situ* EDX; Figure S14). This concentration-dependence is also highlighted by crack formation, as observed by SEM in Figure 2. When the upper potential is set to 1.3 V_{RHE} (harsh conditions), the massive dissolution of Ni, evidenced by both ICP-MS (Figure 1) and EDX (Figure S14), is regarded as the predominant cause of morphological evolution within the first tens of CV cycles, and its influence was found to be more pronounced at intermediate Ni contents, where it is not possible to clearly detect the beginning of particle coalescence before the end of Ni dissolution. In fact, for low Ni concentration values, we claim that superficial diffusion of Pt atoms is the main phenomenon leading to the observed decrease in σ_p (Figure 3b). Because of the speed of the applied voltage ramp, together with the massive loss of Ni mass, we assume that Pt diffusion is not clearly detectable in samples with Ni concentrations higher than 10%. From the comparison of ICP-MS and GISAXS data, it was possible to establish that once the profile of the Ni dissolution rate is near the end and the profile of the Pt dissolution rate has approached the constant regime, particle coalescence was found to be the predominant phenomenon inducing catalyst coarsening. Here, the thickness of the Pt–Ni samples is reduced and the growth of the particles develops mainly along the lateral direction, in agreement with our previous studies.^{30,36} This can be attributed to the weakening of the bond between the catalyst particles and the carbon support due to carbon corrosion, which is inevitable at cycling to 1.3 V_{RHE} and could increase the mobility of catalyst particles and their subsequent coalescence at earlier stages of cycling.^{14,49,50} However, clear markers of neither carbon corrosion nor particle detachment could be identified. In fact, as previously reported, carbon corrosion can also be responsible for particle detachment.¹³ Nonetheless, the reduction of the forwarded scattering probability (I_p , Figure S10a), which is expected to be observed in the case of loss of material from the analyzed area, was not detected. It is also noteworthy that the fact that the scattering length density of carbon is very low compared to that of platinum makes it impossible to follow morphological changes of the carbon support caused by its corrosion using *in situ* GISAXS. On the

other hand, nanoparticle coalescence could also be enhanced by the usage of the nanoparticle-made thin film, where catalyst nanoparticles are in close proximity to each other. During coalescence, the merging of nanoparticles results in an increase of interparticle distance, and as a consequence, Ostwald ripening becomes a more favorable phenomenon.¹³ Overall, the transition points between dissolution and coalescence and between coalescence and Ostwald ripening were found to be inversely proportional to the Ni concentration.

Real carbon supports such as Vulcan have a low amount of pore space and, therefore, have the majority of catalyst nanoparticles on the carbon surface.^{13,51} This leads to lower interparticle distances, especially at higher loadings, and a much different environment from the high-surface-area carbons such as Ketjen. It has recently been suggested by Yu *et al.*, based on postmortem TEM analysis, that the majority of the coarsening events were determined to be coalescence and not Ostwald ripening for PtCo nanoparticles supported on Vulcan,²³ while Padgett *et al.* showed that the primary degradation mechanism of PtCo on Ketjen is Ostwald ripening due to the protection of the nanoparticles from migration, by their position within the carbon support pores.⁵² The lower-surface-area Vulcan is much more similar to the planar carbon substrate used in this study, where we have shown that both coalescence and Ostwald ripening take place and may actually occur simultaneously depending on the catalyst composition and the extent of potential cycling. This can be attributed to the fact that some degradation mechanisms can actually take place in the initial stages and can be hidden due to the lack of techniques that can follow morphological evolution *in situ* and with very high statistical accuracy.

■ CONCLUSIONS

In this work, we have developed a strict methodology for experimental decoupling between catalyst degradation processes at the time scale by means of *in situ* electrochemical GISAXS, complemented by ICP-MS, on a Pt–Ni model ORR catalyst, which represents a promising alternative to bare Pt cathode electrodes in PEMFCs. More specifically, we were able to resolve the time-dependent contribution of the main degradation mechanisms during the initial stages of catalyst degradation as a function of the upper potential and the catalyst composition. The study evidenced the influence of Ni dissolution when the upper potential is set to 1.0 V_{RHE} . The dissolution of the less noble metal induces crack formation in the nanoparticle film until the Pt skeleton remains exposed to the electrolyte, preventing further morphological modification and Ni dissolution. The system reaches a stable condition later for larger values of Ni concentration in the Pt–Ni alloy. When the upper potential is set to 1.3 V_{RHE} , several processes take place: depending on the alloy composition, the dissolution of Ni, together with the Pt redistribution take place at early stages of cycling. Subsequently, particle coalescence becomes the predominant phenomenon in between 10 and 100 CV cycles, with a nonlinear dependence on the Ni concentration. Finally, after several hundred CV cycles, Ostwald ripening becomes predominant with the exception of the intermediate values of the Ni content, where ripening and coalescence were found to coexist evenly.

The accuracy of GISAXS allowed us to precisely describe the evolution of the most important morphological parameters with high precision and to discriminate the dominant effects involved in the catalyst degradation under the given

conditions. Even though compositional variations in $\text{Pt}_x\text{Ni}_{100-x}$ are generally consistent with previously reported findings, our results provide never-before-reported insights into the time-evolution interplay between the main concurrent degradation mechanisms, revealing a clear picture of the electrochemical behavior of bimetallic alloys under fuel-cell-related conditions. It should also be highlighted that the well-defined electrochemical interface used in this study differs from real-world electrocatalysts, which are far more complex, having unevenly distributed ionomers around catalytic particles and a porous carbon support, together forming the so-called three-phase boundary. There, the catalyst behavior is likely to be sensitive to many factors like the initial particle size, interparticle distances, carbon support morphology, etc. Nevertheless, the findings described here represent a background for future work that will address catalyst deterioration on applied systems.

■ MATERIALS AND METHODS

Sample Preparation. The Pt–Ni model catalysts were prepared by means of magnetron cosputtering from 2 in. Pt (99.99% Safina) and 2 in. Ni (99.99% Kurt J. Lesker) targets. Targets were facing the substrate at the angle of 45° while retaining the mutual angle of 90° . The sputtering was carried out in 0.5 Pa of an Ar atmosphere in the constant power mode by applying different powers for Pt and Ni targets. The total sputtering time was 3.5 min, resulting in the formation of 10 nm thick films of $\text{Pt}_x\text{Ni}_{100-x}$ nanoparticles.

The Pt–Ni model catalysts were deposited on a silicon Si(111) wafer (ON Semiconductor) substrate precovered by a 10 nm carbon layer. The carbon layer was deposited using magnetron sputtering from a 4 in. graphite target (Kurt J. Lesker, purity of 99.999%) by applying a DC power of 300 W in 0.5 Pa of an Ar atmosphere.

Sample composition was checked from as-deposited samples via XRD, as reported in Figure S15, together with a comparison of the GISAXS horizontal and vertical cuts of the samples in as-deposited conditions. A more detailed characterization of as-deposited catalysts can be found in our previous work.³⁰

Scanning Electron Microscopy (SEM). SEM images were taken on a Tescan MIRA 3 microscope operated with an electron beam energy of 30 keV.

Energy-Dispersive X-ray Spectroscopy (EDX). The bulk element composition of the as-deposited samples was determined by EDX using a Bruker XFlash detector attached directly to the SEM.

X-ray Diffraction (XRD). XRD measurements were performed using a Rigaku SmartLab diffractometer equipped with a 9 kW rotating-anode X-ray source (Cu $K\alpha$ radiation, $\lambda = 0.15418$ nm), a parabolic multilayer mirror in the primary beam, a set of axial divergence eliminating Soller slits in both incident and diffracted beams (acceptance 5°), and a HighPix-3000 2D hybrid pixel single-photon counting detector. The XRD measurements were done in the parallel beam geometry, glancing angle X-ray diffraction geometry (GAXRD), with a parallel beam Soller slit collimator (acceptance 0.5°) in the diffracted beam. A constant angle of 0.6° for the incidence beam was used for the measurements. The diffraction pattern was fitted by the whole powder pattern refinement method (Rietveld method) using MStruct software.⁵³

Electrochemical Scanning Flow Cell (SFC) with an Inductively Coupled Plasma Mass Spectrometer (ICP-

MS). Electrochemical transient dissolution of ^{195}Pt and ^{60}Ni was monitored on the previously described SFC-ICP-MS system.^{54,55} Saturated Ag/AgCl (Metrohm) and a graphite rod were used as reference and counter electrodes, respectively. The working electrode contact area was approximately 1.1 mm^2 . Freshly prepared 0.1 M H_2SO_4 from 96% sulfuric acid (Suprapur, Merck) and ultrapure water (Milli-Q IQ 7000, Merck) was used as the electrolyte with a flow rate from 20S to $235\ \mu\text{L}\cdot\text{min}^{-1}$ with continuous argon purging. Potentiodynamic cycling was performed from $0.3\ V_{\text{RHE}}$ to different upper potentials (1.0 and $1.3\ V_{\text{RHE}}$) at $500\ \text{mV/s}$ sweep rate. The flow rate varied as the pump tubing aged and was measured regularly. Dissolution was monitored on the NexION 300 (Perkin Elmer) ICP-MS via daily calibration from Pt and Ni solutions (Certipur, Merck), while $10\ \mu\text{g}\cdot\text{L}^{-1}\ ^{187}\text{Re}$ and $20\ \mu\text{g}\cdot\text{L}^{-1}\ ^{59}\text{Co}$ were used as internal standards for ^{195}Pt and ^{60}Ni , respectively. Total quantities of dissolution were obtained via integration of the transient dissolution profiles over time using the measured flow rates.

Grazing-Incidence Small-Angle X-ray Scattering (GISAXS). Two-dimensional GISAXS patterns were recorded at the Austrian SAXS beamline at the ELETTRA synchrotron in Trieste, Italy.⁵⁶ The incident X-ray beam was characterized by a wavelength of $1.54\ \text{\AA}$ (8 keV). The sample was placed in an electrochemical cell dedicated to *in situ* GISAXS electrochemistry³⁶ and connected to a potentiostat (SP-240, Biologic). The Pt wire as a counter electrode (Safina, 99.99%) and the leak-free Ag/AgCl as a reference electrode (LF-1-100, Alvatek)⁵⁷ were used. Potentiodynamic cycling was performed in deaerated 0.1 M H_2SO_4 solution from $0.3\ V_{\text{RHE}}$ to different upper potentials (1.0 and $1.3\ V_{\text{RHE}}$) at $500\ \text{mV/s}$ sweep rate. The sample was placed at a distance of 109.15 cm from a pixel detector (Pilatus 1 M for GISAXS). The stage at which the cell was fixed allowed us to set the incidence angle to 0.6° above the surface. Calibration was performed with Ag-behenate as a reference pattern for the GISAXS detector. For every sample, an image of the dry sample had been taken at first; then, 0.1 M H_2SO_4 solution was injected into the cell and cycled voltammetry measurements were recorded. Two series of seven Pt–Ni samples with increasing Ni content (0, 10, 25, 40, 50, 60, and 75%) were measured per two different values of upper potential (1.0 and $1.3\ V_{\text{RHE}}$). The exposure time was equal to 60 s and repeated after predefined cycle numbers ranging from 0 to 1500 CV. The Austrian SAXS beamline operates with a flux density on the order of $7.5 \times 10^{11}\ \text{ph/s}/\text{mm}^2$, and the experiments were performed in a liquid layer of 3 mm and under grazing-incidence conditions; therefore, radiation damage can be neglected in this setup.

IGOR Pro was used for data reduction and fitting. Two cuts were calculated: the horizontal one (defining the in-plane contributions), at the height of the Yoneda wings, and the vertical one (defining the out-of-plane ones) at specular conditions. For a qualitative analysis, the SAXS correlation length^{46,47} was calculated from both cuts. Scattering correlation length ξ is defined as the mean width of the correlation function $\gamma_0(r)$ ^{46,47} among the bodies that are scattering X-rays, and it can be used as a qualitative marker of the evolution of their size. As a qualitative descriptor of changes derived from scattering patterns, the ratio between the first and the second moment of the scattering curve has been used by integrating over the limited experimental q -range:^{46,47}

$$\xi = \pi \int_{q_{\min}}^{q_{\max}} I(q) q \, dq / \int_{q_{\min}}^{q_{\max}} I(q) q^2 \, dq.$$

Even though it is not

calculated over the entire q -range (i.e., from 0 to infinity), the used quantity for the correlation length ξ is extremely sensitive to structural changes in the probed q -range.⁵⁸ For a quantitative analysis, horizontal cuts were fit by means of the so-called analytical model, which was developed and validated in our previous work.³⁰ Pt nanoparticles are modeled with a product of a form factor by a structure factor: $I(q) \propto I_p P(q, D_p, \sigma_p) S(q, R_{\text{SHS}}, \varphi_{\text{SHS}} \epsilon)$. The form factor is composed of a set of polydispersed spheres, whose size distribution follows a Schultz distribution,^{59,60} which is characterized by the forwarded scattering probability of Pt nanoparticles, I_p , by the mean particle diameter D_p , and by the root-mean-square deviation from the mean particle diameter, σ_p . σ_p is defined as⁶⁰ $\sigma_p = \rho^* D_p$, where ρ is the particle polydispersity index; σ_p is also connected to the parameter Z (which is related to the shape of the distribution) as⁵⁹ $\sigma_p = D_p / (Z + 1)^{1/2}$. As a note, the use of a more appropriate core-shell model would result in a modification of the dimension of the Guinier radius of 10%, whose minor effect was neglected in considering the influence of the size distribution and the available data quality. From these three parameters, particle volume fraction φ_p and number size distribution $D_n(D)$ were determined. From $D_n(D)$, the skewness ν of the probability distribution function was evaluated with the standardized third momentum of the distribution: $\nu = (E[D^3] - 3\overline{D_p}\sigma^2 - \overline{D_p}^3) / \sigma^3$; here, $E[D^3] = \int D_n(D) D_p^3 dD$, $\overline{D_p}$ is the mean value of the distribution and σ represents the root-mean-square deviation. As a structure factor, the sticky hard sphere model^{61,62} was selected. Usually, the hard sphere model is used to describe a multibody system characterized by a short range order and a radial distribution function developing over nearest neighbor particles. In addition, the interaction potential of the sticky hard sphere model differs from the interaction potential of the more simple hard sphere model, by the presence of a potential well, which takes into account any interactive force (either attractive or repulsive) among neighboring particles. The minimum interparticle distance is related to the position of the asymptotic border of the potential well, and it was calculated as $d_{p,\text{min}} = 2^* R_{\text{SHS}}$. The so-called apparent volume fraction φ_{SHS} is related to the probability of finding a nearest neighbor particle, while the depth of the potential well (ϵ) is related to the strength of the interaction and was monitored as obtained.

The analytical model allows one to easily observe the evolution of Pt nanoparticles, but it does not allow one to describe crack formation. In fact, due to their large size, cracks exceed experimental resolution. Concerning the vertical cut, the second and the third bump of the Kiessig fringes⁴³ were singularly fitted by means of a Gaussian peak with a power law as a background. From the position of these peaks, the thickness of the bimetallic layer can be estimated as $t_{\text{Pt}} \cong 2\pi / \Delta q_i$,^{44,45} where $\Delta q = |q_2 - q_3|$, with q_x defining the position of the x_{th} peak.

■ ASSOCIATED CONTENT

SI Supporting Information


The Supporting Information is available free of charge at <https://pubs.acs.org/doi/10.1021/acscatal.1c01111>.

Preliminary sample characterization and supporting figures (PDF)

■ AUTHOR INFORMATION

Corresponding Authors

Heinz Amenitsch – Graz University of Technology, Institute for Inorganic Chemistry, 8010 Graz, Austria; Phone: +43 316 873 32146; Email: amenitsch@tugraz.at; Fax: +43 316 873 32102


Ivan Khalakhan – Charles University, Faculty of Mathematics and Physics, Department of Surface and Plasma Science, 18000 Prague 8, Czech Republic; ; Phone: +420 22191 2321;


Email: ivan.khalakhan@mff.cuni.cz; Fax: +420 22191 2297


Authors

Marco Bogar – CERIC-ERIC c/o Elettra Synchrotron, 34149 Trieste, Italy; Graz University of Technology, Institute for Inorganic Chemistry, 8010 Graz, Austria

Yurii Yakovlev – Charles University, Faculty of Mathematics and Physics, Department of Surface and Plasma Science, 18000 Prague 8, Czech Republic

Daniel John Seale Sandbeck – Helmholtz-Institute Erlangen-Nürnberg for Renewable Energy (IEK-11), Forschungszentrum Jülich GmbH, 91058 Erlangen, Germany; Department of Chemical and Biological Engineering, Friedrich-Alexander-Universität Erlangen-Nürnberg, 91058 Erlangen, Germany; 

Serhiy Cherevko – Helmholtz-Institute Erlangen-Nürnberg for Renewable Energy (IEK-11), Forschungszentrum Jülich GmbH, 91058 Erlangen, Germany; 

Iva Matolínová – Charles University, Faculty of Mathematics and Physics, Department of Surface and Plasma Science, 18000 Prague 8, Czech Republic; 

Notes

The authors declare no competing financial interest.

■ ACKNOWLEDGMENTS

The work was supported by the structural fund project No. CZ.02.1.01/0.0/0.0/16_025/0007414. The authors further acknowledge the CERIC-ERIC Consortium for the access to experimental facilities and financial support. Part of this work was carried out in the frame of the CERIC-ERIC internal project CEROP. In particular, M.B. is very grateful to CERIC-ERIC for his grant in the framework of CEROP. M.B. is very grateful for financial support from the project RETINA, which is being implemented and cofinanced by the European Union–European Regional Development Fund in the frame of the Cooperation Programme Interreg V-A Slovenia-Austria during the program period 2014–2020.

■ REFERENCES

- (1) Greeley, J.; Stephens, I. E. L.; Bondarenko, A. S.; Johansson, T. P.; Hansen, H. A.; Jaramillo, T. F.; Rossmeisl, J.; Chorkendorff, I.; Nørskov, J. K. Alloys of Platinum and Early Transition Metals as Oxygen Reduction Electrocatalysts. *Nat. Chem.* **2009**, *1*, 552–556.
- (2) Stamenkovic, V. R.; Mun, B. S.; Arenz, M.; Mayrhofer, K. J. J.; Lucas, C. A.; Wang, G.; Ross, P. N.; Markovic, N. M. Trends in

Electrocatalysis on Extended and Nanoscale Pt-Bimetallic Alloy Surfaces. *Nat. Mater.* **2007**, *6*, 241–247.

(3) Sievers, G. W.; Jensen, A. W.; Quinson, J.; Zana, A.; Bizzotto, F.; Oezaslan, M.; Dworzak, A.; Kirkensgaard, J. J. K.; Smitsshuysen, T. E. L.; Kadkhodazadeh, S.; Juelscholt, M.; Jensen, K. M. Ø.; Anklam, K.; Wan, H.; Schäfer, J.; Čépe, K.; Escudero-Escribano, M.; Rossmeisl, J.; Quade, A.; Brüser, V.; Arenz, M. Self-Supported Pt–CoO Networks Combining High Specific Activity with High Surface Area for Oxygen Reduction. *Nat. Mater.* **2021**, *20*, 208–213.

(4) Bu, L.; Ding, J.; Guo, S.; Zhang, X.; Su, D.; Zhu, X.; Yao, J.; Guo, J.; Lu, G.; Huang, X. A General Method for Multimetallic Platinum Alloy Nanowires as Highly Active and Stable Oxygen Reduction Catalysts. *Adv. Mater.* **2015**, *27*, 7204–7212.

(5) Wang, C.; Chi, M.; Li, D.; Van Der Vliet, D.; Wang, G.; Lin, Q.; F Mitchell, J.; More, K. L.; Markovic, N. M.; Stamenkovic, V. R. Synthesis of Homogeneous Pt-Bimetallic Nanoparticles as Highly Efficient Electrocatalysts. *ACS Catal.* **2011**, *1*, 1355–1359.

(6) Stamenkovic, V. R.; Fowler, B.; Mun, B. S.; Wang, G.; Ross, P. N.; Lucas, C. A.; Markovic, N. M. Improved Oxygen Reduction Activity on Pt₃Ni(111) via Increased Surface Site Availability. *Science* **2007**, *315*, 493–497.

(7) Dubau, L.; Lopez-Haro, M.; Castanheira, L.; Durst, J.; Chatenet, M.; Bayle-Guillemaud, P.; Guétaz, L.; Caqué, N.; Rossinot, E.; Maillard, F. Probing the Structure, the Composition and the ORR Activity of Pt₃Co/C Nanocrystallites during a 3422h PEMFC Ageing Test. *Appl. Catal., B* **2013**, *142–143*, 801–808.

(8) Khalakhan, I.; Vega, L.; Vorokhta, M.; Skála, T.; Viñes, F.; Yakovlev, Y. V.; Neyman, K. M.; Matolínová, I. Irreversible Structural Dynamics on the Surface of Bimetallic PtNi Alloy Catalyst under Alternating Oxidizing and Reducing Environments. *Appl. Catal., B* **2020**, *264*, No. 118476.

(9) Khalakhan, I.; Vorokhta, M.; Kúš, P.; Dopita, M.; Václavů, M.; Fiala, R.; Tsud, N.; Skála, T.; Matolín, V. In Situ Probing of Magnetron Sputtered Pt-Ni Alloy Fuel Cell Catalysts during Accelerated Durability Test Using EC-AFM. *Electrochim. Acta* **2017**, *245*, 760–769.

(10) Khalakhan, I.; Vorokhta, M.; Václavů, M.; Šmíd, B.; Lavková, J.; Matolínová, I.; Fiala, R.; Tsud, N.; Skála, T.; Matolín, V. In-Situ Electrochemical Atomic Force Microscopy Study of Aging of Magnetron Sputtered Pt-Co Nanoalloy Thin Films during Accelerated Degradation Test. *Electrochim. Acta* **2016**, *211*, 52–58.

(11) Maillard, F.; Dubau, L.; Durst, J.; Chatenet, M.; André, J.; Rossinot, E. Durability of Pt₃Co/C Nanoparticles in a Proton-Exchange Membrane Fuel Cell: Direct Evidence of Bulk Co Segregation to the Surface. *Electrochem. Commun.* **2010**, *12*, 1161–1164.

(12) Chen, S.; Gasteiger, H. A.; Hayakawa, K.; Tada, T.; Shao-Horn, Y. Platinum-Alloy Cathode Catalyst Degradation in Proton Exchange Membrane Fuel Cells: Nanometer-Scale Compositional and Morphological Changes. *J. Electrochem. Soc.* **2010**, *157*, A82–A97.

(13) Meier, J. C.; Galeano, C.; Katsounaros, I.; Witte, J.; Bongard, H. J.; Topalov, A. A.; Baldizzone, C.; Mezzavilla, S.; Schüth, F.; Mayrhofer, K. J. J. Design Criteria for Stable Pt/C Fuel Cell Catalysts. *Beilstein J. Nanotechnol.* **2014**, *5*, 44–67.

(14) Meier, J. C.; Galeano, C.; Katsounaros, I.; Topalov, A. A.; Kostka, A.; Schüth, F.; Mayrhofer, K. J. J. Degradation Mechanisms of Pt/C Fuel Cell Catalysts under Simulated Start-Stop Conditions. *ACS Catal.* **2012**, *2*, 832–843.

(15) Cheng, L.; Khedekar, K.; Rezaei Talarposhti, M.; Perego, A.; Metzger, M.; Kuppan, S.; Stewart, S.; Atanassov, P.; Tamura, N.; Craig, N.; Zenyuk, I. V.; Johnston, C. M. Mapping of Heterogeneous Catalyst Degradation in Polymer Electrolyte Fuel Cells. *Adv. Energy Mater.* **2020**, *10*, No. 2000623.

(16) Erlebacher, J.; Aziz, M. J.; Karma, A.; Dimitrov, N.; Sieradzki, K. Evolution of Nanoporosity in Dealloying. *Nature* **2001**, *410*, 450–453.

(17) Wang, C.; Chi, M.; Wang, G.; Van Der Vliet, D.; Li, D.; More, K.; Wang, H. H.; Schlueter, J. A.; Markovic, N. M.; Stamenkovic, V. R. Correlation between Surface Chemistry and Electrocatalytic Proper-

ties of Monodisperse Pt_xNi_{1-x} Nanoparticles. *Adv. Funct. Mater.* **2011**, *21*, 147–152.

(18) Cai, Y.; Kongkanand, A.; Gu, W.; Moylan, T. E. Effects of Cobalt Cation on Low Pt-Loaded PEM Fuel Cell Performance. *ECS Trans.* **2015**, *69*, 1047–1061.

(19) Braaten, J.; Kongkanand, A.; Litster, S. Oxygen Transport Effects of Cobalt Cation Contamination of Ionomer Thin Films in Proton Exchange Membrane Fuel Cells. *ECS Trans.* **2017**, *80*, 283–290.

(20) Xin, H. L.; Mundy, J. A.; Liu, Z.; Cabezas, R.; Hovden, R.; Kourkoutis, L. F.; Zhang, J.; Subramanian, N. P.; Makharia, R.; Wagner, F. T.; Muller, D. A. Atomic-Resolution Spectroscopic Imaging of Ensembles of Nanocatalyst Particles across the Life of a Fuel Cell. *Nano Lett.* **2012**, *12*, 490–497.

(21) Yu, C.; Holby, E. F.; Yang, R.; Toney, M. F.; Morgan, D.; Strasser, P. Growth Trajectories and Coarsening Mechanisms of Metal Nanoparticle Electrocatalysts. *ChemCatChem* **2012**, *4*, 766–770.

(22) Khalakhan, I.; Choukourou, A.; Vorokhta, M.; Kúš, P.; Matolínová, I.; Matolín, V. In Situ Electrochemical AFM Monitoring of the Potential-Dependent Deterioration of Platinum Catalyst during Potentiodynamic Cycling. *Ultramicroscopy* **2018**, *187*, 64–70.

(23) Yu, Y.; Xin, H. L.; Hovden, R.; Wang, D.; Rus, E. D.; Mundy, J. A.; Muller, D. A.; Abruña, H. D. Three-Dimensional Tracking and Visualization of Hundreds of Pt-Co Fuel Cell Nanocatalysts during Electrochemical Aging. *Nano Lett.* **2012**, *12*, 4417–4423.

(24) Shao-Horn, Y.; Sheng, W. C.; Chen, S.; Ferreira, P. J.; Holby, E. F.; Morgan, D. Instability of Supported Platinum Nanoparticles in Low-Temperature Fuel Cells. *Top. Catal.* **2007**, *46*, 285–305.

(25) Granqvist, C. G.; Buhrman, R. A. Size Distributions for Supported Metal Catalysts: Coalescence Growth versus Ostwald Ripening. *J. Catal.* **1976**, *42*, 477–479.

(26) Ahluwalia, R. K.; Arisetty, S.; Peng, J.-K.; Subbaraman, R.; Wang, X.; Kariuki, N.; Myers, D. J.; Mukundan, R.; Borup, R.; Polevaya, O. Dynamics of Particle Growth and Electrochemical Surface Area Loss Due to Platinum Dissolution. *J. Electrochem. Soc.* **2014**, *161*, F291–F304.

(27) Gilbert, J. A.; Kariuki, N. N.; Subbaraman, R.; Kropf, J. A.; Smith, M. C.; Holby, E. F.; Morgan, D.; Myers, D. J. In Situ Anomalous Small-Angle X-ray Scattering Studies of Platinum Nanoparticle Fuel Cell Electrocatalyst Degradation. *J. Am. Chem. Soc.* **2012**, *134*, 14823–14833.

(28) Smith, M. C.; Gilbert, J. A.; Mawdsley, J. R.; Seifert, S.; Myers, D. J. In Situ Small-Angle X-Ray Scattering Observation of Pt Catalyst Particle Growth during Potential Cycling. *J. Am. Chem. Soc.* **2008**, *130*, 8112–8113.

(29) Ruge, M.; Drnec, J.; Rahn, B.; Reikowski, F.; Harrington, D. A.; Carlà, F.; Felici, R.; Stettner, J.; Magnussen, O. M. Structural Reorganization of Pt(111) Electrodes by Electrochemical Oxidation and Reduction. *J. Am. Chem. Soc.* **2017**, *139*, 4532–4539.

(30) Khalakhan, I.; Bogar, M.; Vorokhta, M.; Kúš, P.; Yakovlev, Y.; Dopita, M.; Sandbeck, D. J. S.; Cherevko, S.; Matolínová, I.; Amenitsch, H. Evolution of the PtNi Bimetallic Alloy Fuel Cell Catalyst under Simulated Operational Conditions. *ACS Appl. Mater. Interfaces* **2020**, *12*, 17602–17610.

(31) Tuavev, X.; Rudi, S.; Petkov, V.; Hoell, A.; Strasser, P. In Situ Study of Atomic Structure Transformations of Pt-Ni Nanoparticle Catalysts during Electrochemical Potential Cycling. *ACS Nano* **2013**, *7*, 5666–5674.

(32) Bergmann, A.; Roldan Cuenya, B. Operando Insights into Nanoparticle Transformations during Catalysis. *ACS Catal.* **2019**, *9*, 10020–10043.

(33) Datye, A. K.; Xu, Q.; Kharas, K. C.; McCarty, J. M. Particle Size Distributions in Heterogeneous Catalysts: What Do They Tell Us about the Sintering Mechanism? *Catal. Today* **2006**, *111*, 59–67.

(34) Khalakhan, I.; Supik, L.; Vorokhta, M.; Yakovlev, Y.; Dopita, M.; Sandbeck, D. J. S.; Cherevko, S.; Veltruská, K.; Matolínová, I. Compositionally Tuned Magnetron Co-Sputtered Pt_xNi_{100-x} Alloy

as a Cathode Catalyst for Proton Exchange Membrane Fuel Cells. *Appl. Surf. Sci.* **2020**, *511*, No. 145486.

(35) Pizzutilo, E.; Geiger, S.; Grote, J.-P.; Mingers, A.; Mayrhofer, K. J. J.; Arenz, M.; Cherevko, S. On the Need of Improved Accelerated Degradation Protocols (ADPs): Examination of Platinum Dissolution and Carbon Corrosion in Half-Cell Tests. *J. Electrochem. Soc.* **2016**, *163*, F1510–F1514.

(36) Bogar, M.; Khalakhan, I.; Gambitta, A.; Yakovlev, Y.; Amenitsch, H. In Situ Electrochemical Grazing Incidence Small Angle X-Ray Scattering: From the Design of an Electrochemical Cell to an Exemplary Study of Fuel Cell Catalyst Degradation. *J. Power Sources* **2020**, *477*, No. 229030.

(37) Pourbaix, M.; Zhang, H.; Pourbaix, A. Presentation of an Atlas of Chemical and Electrochemical Equilibria in the Presence of a Gaseous Phase. *Mater. Sci. Forum* **1997**, *251–254*, 143–148.

(38) Cherevko, S. Electrochemical Dissolution of Noble Metals Native Oxides. *J. Electroanal. Chem.* **2017**, *787*, 11–13.

(39) Baldizzone, C.; Gan, L.; Hodnik, N.; Keeley, G. P.; Kostka, A.; Heggen, M.; Strasser, P.; Mayrhofer, K. J. J. Stability of Dealloyed Porous Pt/Ni Nanoparticles. *ACS Catal.* **2015**, *5*, 5000–5007.

(40) Zhang, G. R.; Wolker, T.; Sandbeck, D. J. S.; Munoz, M.; Mayrhofer, K. J. J.; Cherevko, S.; Etzold, B. J. M. Tuning the Electrocatalytic Performance of Ionic Liquid Modified Pt Catalysts for the Oxygen Reduction Reaction via Cationic Chain Engineering. *ACS Catal.* **2018**, *8*, 8244–8254.

(41) George, M.; Zhang, G. R.; Schmitt, N.; Brunnengräber, K.; Sandbeck, D. J. S.; Mayrhofer, K. J. J.; Cherevko, S.; Etzold, B. J. M. Effect of Ionic Liquid Modification on the ORR Performance and Degradation Mechanism of Trimetallic PtNiMo/C Catalysts. *ACS Catal.* **2019**, *9*, 8682–8692.

(42) Topalov, A. A.; Cherevko, S.; Zeradjanin, A. R.; Meier, J. C.; Katsounaros, I.; Mayrhofer, K. J. J. Towards a Comprehensive Understanding of Platinum Dissolution in Acidic Media. *Chem. Sci.* **2014**, *5*, 631–638.

(43) Kiessig, H. Untersuchungen Zur Totalreflexion von Röntgenstrahlen. *Ann. Phys.* **1931**, *402*, 715–768.

(44) Gibaud, A.; Hazra, S. X-Ray Reflectivity and Diffuse Scattering. *Curr. Sci.* **2000**, *78*, 1467–1477.

(45) Pietsch, U.; Holy, V.; Baumbach, T. *High-Resolution X-Ray Scattering: From Thin Films to Lateral Nanostructures*, 2nd ed; Springer-Verlag, 2004; p 408.

(46) Glatter, O.; Kratky, O. *Small Angle X-Ray Scattering*; Academic Press, 1982; p 515.

(47) Glatter, O. *Scattering Methods and Their Application in Colloid and Interface Science*; Elsevier, 2018; p 392.

(48) Povia, M.; Herranz, J.; Binninger, T.; Nachttegaal, M.; Diaz, A.; Kohlbrecher, J.; Abbott, D. F.; Kim, B. J.; Schmidt, T. J. Combining SAXS and XAS to Study the Operando Degradation of Carbon-Supported Pt-Nanoparticle Fuel Cell Catalysts. *ACS Catal.* **2018**, *8*, 7000–7015.

(49) Li, L.; Hu, L.; Li, J.; Wei, Z. Enhanced Stability of Pt Nanoparticle Electrocatalysts for Fuel Cells. *Nano Res.* **2015**, *8*, 418–440.

(50) Beermann, V.; Holtz, M. E.; Padgett, E.; De Araujo, J. F.; Muller, D. A.; Strasser, P. Real-Time Imaging of Activation and Degradation of Carbon Supported Octahedral Pt-Ni Alloy Fuel Cell Catalysts at the Nanoscale Using: In Situ Electrochemical Liquid Cell STEM. *Energy Environ. Sci.* **2019**, *12*, 2476–2485.

(51) Jovanovič, P.; Petek, U.; Hodnik, N.; Ruiz-Zepeda, F.; Gatalo, M.; Šala, M.; Šelih, V. S.; Fellingner, T. P.; Gabersček, M. Importance of Non-Intrinsic Platinum Dissolution in Pt/C Composite Fuel Cell Catalysts. *Phys. Chem. Chem. Phys.* **2017**, *19*, 21446–21452.

(52) Padgett, E.; Yarlagadda, V.; Holtz, M. E.; Ko, M.; Levin, B. D. A.; Kukreja, R. S.; Ziegelbauer, J. M.; Andrews, R. N.; Ilavsky, J.; Kongkanand, A.; Muller, D. A. Mitigation of PEM Fuel Cell Catalyst Degradation with Porous Carbon Supports. *J. Electrochem. Soc.* **2019**, *166*, F198–F207.

(53) Matěj, Z.; Kadlecová, A.; Janeček, M.; Matějová, L.; Dopita, M.; Kužel, R. Refining Bimodal Microstructure of Materials with Mstruct. *Powder Diffr.* **2014**, *29*, S35–S41.

(54) Schuppert, A. K.; Topalov, A. A.; Katsounaros, I.; Klemm, S. O.; Mayrhofer, K. J. J. A Scanning Flow Cell System for Fully Automated Screening of Electrocatalyst Materials. *J. Electrochem. Soc.* **2012**, *159*, F670–F675.

(55) Cherevko, S.; Topalov, A. A.; Zeradjanin, A. R.; Keeley, G. P.; Mayrhofer, K. J. J. Temperature-Dependent Dissolution of Polycrystalline Platinum in Sulfuric Acid Electrolyte. *Electrocatalysis* **2014**, *5*, 235–240.

(56) Amenitsch, H.; Bernstorff, S.; Kriechbaum, M.; Lombardo, D.; Mio, H.; Rappolt, M.; Laggner, P. Performance and First Results of the ELETTRA High-Flux Beamline for Small-Angle X-Ray Scattering. *J. Appl. Crystallogr.* **1997**, *30*, 872–876.

(57) Leak-Free Electrodes. <https://www.alvatek.co.uk/leak-free-electrodes/>.

(58) Ehmman, H. M. A.; Werzer, O.; Pachmajer, S.; Mohan, T.; Amenitsch, H.; Resel, R.; Kornherr, A.; Stana-Kleinschek, K.; Kontturi, E.; Spirk, S. Surface-Sensitive Approach to Interpreting Supramolecular Rearrangements in Cellulose by Synchrotron Grazing Incidence Small-Angle X-Ray Scattering. *ACS Macro Lett.* **2015**, *4*, 713–716.

(59) Kotlarchyk, M.; Chen, S. H. Analysis of Small Angle Neutron Scattering Spectra from Polydisperse Interacting Colloids. *J. Chem. Phys.* **1983**, *79*, 2461–2469.

(60) Kotlarchyk, M.; Stephens, R. B.; Huang, J. S. Study of Schultz Distribution to Model Polydispersity of Microemulsion Droplets. *J. Phys. Chem. A* **1988**, *92*, 1533–1538.

(61) Sharma, R. V.; Sharma, K. C. The Structure Factor and the Transport Properties of Dense Fluids Having Molecules with Square Well Potential, a Possible Generalization. *Phys. A* **1977**, *89*, 213–218.

(62) Pontoni, D.; Finet, S.; Narayanan, T.; Rennie, A. R. Interactions and Kinetic Arrest in an Adhesive Hard-Sphere Colloidal System. *J. Chem. Phys.* **2003**, *119*, 6157–6165.